

## Chapter 5

# CORONAL MAGNETIC FIELD MEASUREMENTS THROUGH GYRORESONANCE EMISSION

Stephen M. White

*Department of Astronomy, University of Maryland*

*College Park MD 20742 USA*

white@astro.umd.edu

**Abstract** This article reviews the use of gyroresonance emission at radio wavelengths to measure coronal magnetic fields. The spiralling motion of electrons in the 200–2000 G fields in the solar corona produces sufficient opacity to render the corona optically thick, making it easy to recognize such sources in microwave images from their coronal brightness temperatures. Where gyroresonance sources are present they may be used as sensitive probes of the magnetic field strength above active regions, and this unique capability is one of the strengths of radio observations. Typically a gyroresonance radio source shows the temperature on an optically thick surface of constant magnetic field within the corona. Since each radio frequency corresponds to a different magnetic field strength, the coronal structure can be “peeled away” by using different frequencies.

**Keywords:** Sun, solar corona, solar magnetic fields, solar radio emission

## Introduction

Since the realization in the early 1960s (Ginzburg & Zheleznyakov 1961; Kakinuma & Swarup 1962; Zheleznyakov 1962) that the strong radio emission observed from solar active regions was associated with gyroresonance opacity, radio observations have provided a direct measurement of magnetic field strengths in the solar corona. It is a happy coincidence that the low harmonics of the range of magnetic field strengths found in the corona (up to 2500 G) correspond to the range of microwave frequencies (1–20 GHz) for which atmospheric transmission is not an issue and high spatial resolution radio observations are

readily feasible. In this review we discuss the ideas behind the use of radio observations to determine the magnetic field strength in the corona.

Both of the mechanisms responsible for opacity in the active region corona at radio wavelengths, gyroresonance emission and bremsstrahlung (free electrons deflected by ions and remaining unbound, hence also known as free-free emission), are sensitive to the magnetic field. Bremsstrahlung emission in a magnetic field is polarized because the magnetic field breaks the degeneracy in properties of the two natural wave modes, so that information on the field is contained only in the polarized signal. In gyroresonance emission the effect is much more direct: it is the acceleration of electrons by the  $\mathbf{v} \times \mathbf{B}$  magnetic force itself which produces the opacity, so that each polarization by itself independently contains information on the magnetic field. Thus bremsstrahlung and gyroresonance emission provide quite different diagnostics. At frequencies below  $\sim 3$  GHz bremsstrahlung tends to dominate active region emission, making the corona optically thick at heights above the gyroresonance layers. At these low frequencies bremsstrahlung is usually the only emission available for coronal magnetic field diagnostics, and the application of bremsstrahlung for these purposes is discussed in Chapter 6, by Gelfreikh. Chapter 13, by Brosius, describes techniques by which both bremsstrahlung and gyroresonance diagnostics can be combined in investigating coronal magnetic fields. Another relevant effect is the change in polarization induced by propagation through the magnetized plasma of the solar atmosphere, discussed in Chapter 7, by Ryabov.

In the next section we briefly contrast the problems of measuring photospheric and coronal magnetic fields, then discuss the basic properties of thermal gyroresonance emission (also known as cyclotron emission), and show how these properties determine the radio appearance of solar active regions. We also discuss some of the limitations of radio observations. Many people have contributed over the years to our understanding of gyroresonance emission from the corona, and we will not attempt to ascribe credit for each specific development. Previous papers covering similar topics include Zlotnik (1968*a, b*), Zheleznyakov (1970), Lantos (1972), Gelfreikh & Lubyshev (1979), Alissandrakis, Kundu & Lantos (1980), Krüger, Hildenbrandt & Fürstenberg (1985), Hurford (1986), Brosius & Holman (1989), Lee, Hurford & Gary (1993), Vourlidas (1996), and White & Kundu (1997).

## 1. Coronal Magnetic Fields are Intrinsically 3D

An important aspect of coronal magnetic fields that needs to be appreciated is that they are intrinsically three dimensional, and this makes their measurement a fundamentally different problem from that of measuring magnetic fields at the solar photosphere. The solar photosphere is a well-defined two-dimensional surface at which the solar atmosphere becomes optically thin to photons at op-

tical wavelengths. To quite a good approximation, the photosphere is spherical: the largest deviations from a sphere occur in the Wilson depressions in the umbrae of large sunspots, which may be several hundred km below the normal radius of the photosphere (e.g., Bray & Loughhead 1964). Thus observations of the Zeeman effect in optical lines can be safely assumed to come from a sharp two-dimensional surface, and the magnetic field strengths measured from such data come from a known height (although often radiative transfer in the lower atmosphere must be taken into account in order to untangle complicated Zeeman profiles). Even in the case of chromospheric and transition region lines, the thickness of the emitting layer is small compared to the transverse dimension of a typical resolution element.

This is far from true in the case of the corona, where densities of  $10^9 \text{ cm}^{-3}$  can be found at heights of  $10^5 \text{ km}$ . One would like to be able to measure the magnetic field strength at all heights along a given line of sight, at least to within the horizontal resolution of the data: a set of coronal magnetic field strength measurements should be three dimensional. It is difficult to see how this can be achieved with optically thin line diagnostics alone, because most of the optical, IR and EUV lines are proportional to the square of the plasma number density and thus are heavily weighted to the brightest emission feature along any given line of sight: this feature will dominate the Zeeman signal in a given pixel and no information on the field strength at other heights can be retrieved. In this case even stereo observations offer little improvement, since each pixel in both images will be dominated by the brightest feature along that line of sight and effectively one can at best double the number of points in the volume at which  $B$  is measured. If we take the notion of the dynamic corona seriously then tomography also offers little help in this regard: it is precisely the fields that change most rapidly that are often most interesting scientifically, but these are the fields for which tomography does not work since it assumes constant fields.

One of the attractions of gyroresonance emission for the measurement of coronal magnetic fields is that it is not optically thin: different magnetic field strengths are optically thick at different frequencies and thus by tuning the frequency we can peel away the corona in a truly three-dimensional nature. The vertical scale height is not easily retrieved from the radio data as we will see, but vertical information is present.

## 2. Extrapolations of Surface Magnetic Fields

In principal, one can determine the coronal magnetic field distribution from the photospheric magnetic field distribution under certain assumptions. Given a complete measurement of the vector magnetic field  $\mathbf{B}$  at a surface, one can solve a boundary value problem for the distribution of  $\mathbf{B}$  throughout the volume above the boundary using the nonlinear equations  $(\nabla \times \mathbf{B}) \times \mathbf{B} = 0$  and

$\nabla \cdot \mathbf{B} = 0$ . Here the assumption that the coronal field is force-free has been made, i.e., these equations are valid for a quasi-static corona in which any  $\mathbf{J} \times \mathbf{B}$  forces perpendicular to magnetic field lines have been allowed to act and the corona has relaxed to a force-free state. In particular, any currents present in the corona must flow along field lines. The evolutionary timescales for the solar magnetic field outside flares and other explosive phenomena involving reconnection in the corona are slow enough that this assumption should be valid most of the time. The system of equations plus a boundary measurement set constitutes a mixed elliptic-hyperbolic boundary value problem which has proven remarkably difficult to solve (Gary 1989; McClymont & Mikić 1994; Amari *et al.* 1999). One can write generally  $\nabla \times \mathbf{B} = \alpha(\mathbf{r})\mathbf{B}$  and solve for the scalar  $\alpha(\mathbf{r})$ , which is constant along field lines since  $\mathbf{B} \cdot \nabla\alpha(\mathbf{r}) = 0$ . Common approximations are the potential approximation ( $\nabla \times \mathbf{B} = 0$ ,  $\mathbf{B} = \nabla\phi$ , where  $\phi$  is a scalar potential), only valid if no currents are present, and the “linear force-free solution” ( $\alpha$  is a constant everywhere). Unfortunately the observations indicate that  $\alpha$  is not a constant in a given coronal region.

Numerical methods for solving the full nonlinear force-free equations have been developed. To ensure a well-posed problem, one needs a measurement of the vertical component of the magnetic field everywhere and the value of  $\alpha(\mathbf{r})$  at the boundary for one polarity. Relaxation techniques have had considerable success at producing an accurate solution to the equations, as judged by comparisons with observed magnetic field lines (Jiao, McClymont, & Mikić 1997) and measured coronal magnetic field strengths (Lee *et al.* 1998), but there are some limitations: the direction of the transverse component of the magnetic field in the corona cannot be determined unambiguously (to within  $180^\circ$ ) (e.g., Semel & Skumanich 1998); errors in measurements of the photospheric magnetic field affect the reconstruction of the coronal field (Klimchuk & Canfield 1994); and the photospheric values of  $\alpha$  may not be appropriate in the corona since the photosphere is not force-free (Metcalf *et al.* 1995). In the future measurements of the chromospheric magnetic field may avoid this latter difficulty.

### 3. The Properties of Gyroresonance Emission

#### 3.1 Physical mechanism

A collisionless plasma such as the solar corona (where a typical collision frequency, e.g., for density  $n_e = 10^{10} \text{ cm}^{-3}$  and temperature  $T = 2 \times 10^6 \text{ K}$ , is 200 Hz) may be characterized by two frequencies corresponding to electron resonances: the frequency of oscillation of electrons in the electric field of the ions, known as the plasma frequency,  $\nu_p = 8980\sqrt{n_e} \text{ Hz}$ ; and the gyro frequency, which is the frequency of rotation of an electron about the magnetic field due to the  $\mathbf{v} \times \mathbf{B}$  Lorentz force,  $\nu_B = 2.80 \times 10^6 B \text{ Hz}$ , where  $B$  is measured in G. For typical conditions in gyroresonant sources above active regions

( $n_e = 10^{10} \text{ cm}^{-3}$  and  $B \gtrsim 300 \text{ G}$ ),  $\nu_B > \nu_p$ . In such a plasma the propagating electromagnetic modes corresponding to the free-space radiation modes are circularly polarized under most conditions. One of the modes, known as the *extraordinary* or *x* mode, gyrates about the magnetic field with the same sense of rotation as an electron, and therefore resonates strongly with the thermal electron population; the other mode, known as the *ordinary* or *o* mode, gyrates about the magnetic field direction with the sense opposite to that of the electron, and correspondingly interacts much less strongly. Since a radio telescope can generally detect both modes independently, as opposite circular polarizations, this difference in the strength of interaction of the two modes provides a powerful diagnostic.

The frequency width of a given cyclotron resonance  $\propto \mu^{-1/2} s \nu_B$ , where  $\mu = m_e c^2 / k_B T$ . Since  $\mu \approx 3000$  in the corona, the cyclotron resonances are very narrow and, for a given value of  $\nu_B$ , opacity is only significant at frequencies very close to discrete harmonics  $s \nu_B$ ,  $s = 1, 2, 3, \dots$  (at much higher temperatures the individual resonances have significant width and may overlap). Equivalently, if we are observing an inhomogeneous corona at a frequency  $\nu$ , gyroresonance opacity is only significant at those discrete points along the line of sight at which  $\nu_B = \nu/s$ ,  $s = 1, 2, 3, \dots$ . The thermal width of the cyclotron resonance at coronal temperatures is such that  $B$  varies by less than 2% across a resonant layer, corresponding to a physical width of less than 200 km for typical coronal magnetic gradients (scale length  $\sim 10^4 \text{ km}$ ). The narrow physical thickness of the gyroresonant layers is an important feature of this mechanism: since they are much smaller than relevant gradients in  $n_e$ ,  $B$  and  $T$  (except possibly in the vicinity of current sheets), these physical properties may be regarded as constant across any given gyroresonant layer.

### 3.2 Opacity

The formal expression for gyroresonance opacity is discussed in many places (Zheleznyakov 1970; Melrose 1980; Robinson & Melrose 1984) and will not be derived here. Instead we will simply quote the expression for the optical depth  $\tau$  of a gyroresonance layer (the absorption coefficient integrated through the layer) as a function of the frequency  $\nu$ , the harmonic number  $s$  (which determines  $\nu_B = \nu/s$  and hence  $B$  in the layer), and the angle  $\theta$  between the magnetic field direction and the line of sight:

$$\tau_{x,o}(s, \nu, \theta) = .0133 \frac{n_e L_B(\theta)}{\nu} \frac{s^2}{s!} \left( \frac{s^2 \sin^2 \theta}{2\mu} \right)^{s-1} F_{x,o}(\theta) \quad (5.1)$$

where  $L_B(\theta)$  is the scale length of the magnetic field ( $B / \frac{\partial B}{\partial l}$ ) evaluated along the line of sight. For simplicity we have set the refractive index to be unity

in (5.1).  $F_{x,o}(\theta)$  is a function of angle which is of order unity for the  $x$  mode near  $\theta = 90^\circ$ , but decreases sharply at smaller  $\theta$ , and is smaller in the  $o$  mode than in the  $x$  mode. At angles  $\theta$  away from  $90^\circ$  it is often approximated by

$$F_{x,o}(\theta) \approx (1 - \sigma \cos \theta)^2 \quad (5.2)$$

with  $\sigma = -1$  for the  $x$  mode and  $\sigma = 1$  for the  $o$  mode. However, this approximation is really only appropriate when the two natural electromagnetic modes are perfectly circularly polarized, and at the low harmonics ( $s = 1, 2, 3, 4$ ) relevant to the corona this is rarely a good assumption. Zlotnik (1968*a*) presents accurate expressions for  $F_{x,o}(\theta)$  which correctly handle the mode polarization properties. (Note that Zlotnik's formulae are presented in the limit that the refractive index is unity, and require a small correction when  $\nu_p \sim \nu_B$ .)

In Figure 5.1 we present exact calculations of  $\tau$ , the optical depth of a gyroresonant layer, for typical coronal conditions ( $T = 3 \times 10^6$  K,  $L_B = 10^9$  cm) and a fixed frequency of 5 GHz at the appropriate harmonics  $s = 2, 3$  and 4. Both the  $x$  (solid lines) and  $o$  (dashed lines) modes are shown. For comparison, we also plot the approximation represented by (5.2) (dotted lines).

A number of features should be noted in this figure:

- For typical coronal conditions, the  $x$  mode is optically thick ( $\tau \geq 1$ ) in the  $s = 2$  and 3 layers over a broad range of angles  $\theta$ . The  $o$  mode is optically thick over most of the  $s = 2$  layer, and may be at least marginally optically thick over a small portion of the  $s = 3$  layer if  $\theta$  is large. Harmonics greater than  $s = 4$  do not have any significant optical depth in the quiet solar corona.
- At each harmonic and angle the  $o$  mode opacity is always at least an order of magnitude smaller than the  $x$  mode opacity, despite the fact that (5.2) predicts that they should be nearly equal for a range of  $\theta$  around  $90^\circ$ . The approximation (5.2) is adequate for the  $x$  mode at small  $\theta$ , but is poor for the  $o$  mode at all  $\theta$ , being easily a factor of 2 or more in error even at small angles.
- The opacity drops sharply towards small  $\theta$  in both modes. At angles very close to  $90^\circ$ , the  $o$  mode opacity dips sharply since it must be a factor of  $\mu$  smaller than the  $x$  mode opacity exactly at  $\theta = 90^\circ$  (e.g., Bornatici *et al.* 1983, Robinson 1991). By (5.1), the opacity is zero at  $\theta = 0^\circ$  for  $s > 1$ . The  $\sin^{2s-2} \theta$ -dependence of (5.1) causes the fall-off towards small  $\theta$  to be much more rapid as  $s$  increases.
- For each increase of  $s$  by 1, the opacity in a given mode at a given angle drops by slightly more than 2 orders of magnitude. This is largely due to the  $\mu^{-s}$  dependence of (5.1). The importance of this large change in

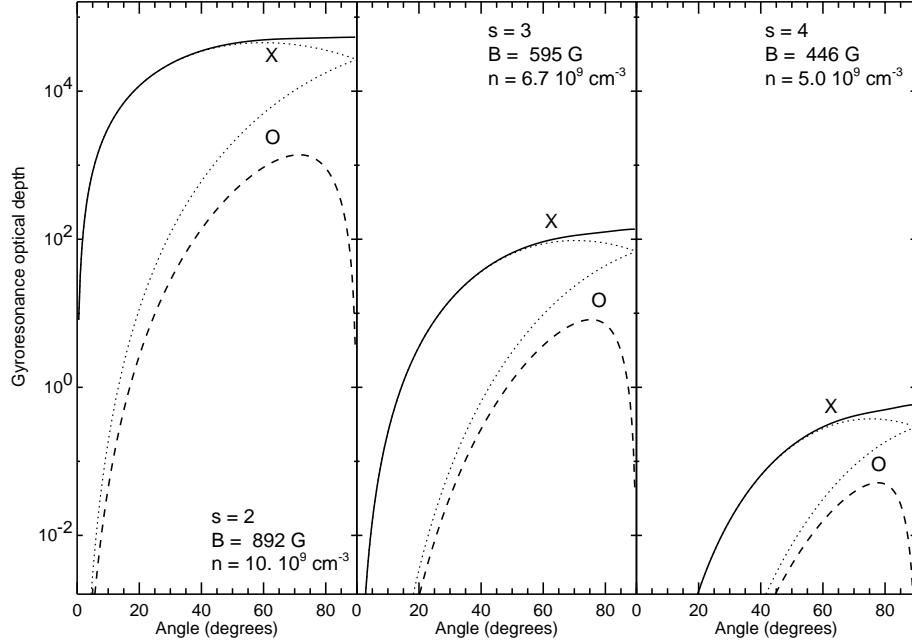


Figure 5.1. The (integrated) optical depth of the  $s = 2, 3, 4$  gyroresonance layers at 5 GHz (left, middle and right panels, respectively) as a function of the angle  $\theta$  between the line of sight and the magnetic field direction. The temperature in the source is  $3 \times 10^6 \text{ K}$ , and the magnetic scale height  $L_B$  is  $10^9 \text{ cm}$ . In each panel the solid line is the optical depth of the layer in the  $x$  mode, and the dashed line is the optical depth in the  $o$  mode. The dotted lines show the optical depth obtained using the circularly-polarized mode approximation (5.2). The density used for this calculation was decreased as  $s$  increases to simulate the decrease of  $n_e$  with height: the values are shown in each panel.

opacity from one layer to the next is that a given harmonic layer is likely to be either optically thick over a wide range of angles  $\theta$ , or else optically thin everywhere.

An important point to be emphasized is that gyroresonance observations are sensitive to the absolute magnetic field strength  $B$ , whereas conventional (Babcock or Leighton style) optical magnetographs measure only the line-of-sight component of the magnetic field,  $B \cos \theta$ , and thus are of limited value for regions near the solar limb. Further, in many cases magnetographs measure magnetic flux averaged over a resolution element (a pixel or a seeing cell) and are thus affected by the filling factor of the magnetic field within the resolution element; radio observations are not affected by this filling factor.

## 4. Gyroresonance Radio Emission from Active Regions

### 4.1 Radio emission from a dipole magnetic field

Here we will use a dipole magnetic field (vertically-oriented and seen looking directly onto one pole, often used as a model for isolated sunspots) to illustrate the ways in which the properties of gyroresonance emission affect the appearance of solar active regions at microwave frequencies. Figure 5.2 shows the expected appearance of a perfectly dipolar field (of peak surface field strength 2500 G) at a frequency of 5 GHz. The upper panel shows the four lowest gyroresonant layers ( $s = 1, 2, 3, 4$ , corresponding to  $B = 1785, 892, 595$  and  $446$  G, respectively), with the line-type indicating whether the layer is optically thick in a given mode. A solid line in the upper panel indicates that the layer is optically thick at both  $x$  and  $o$  modes; a dashed line indicates that only the  $x$  mode is optically thick; and a thin dotted line represents a region of the layer optically thin in both modes. The thin solid lines are magnetic field lines. In the bottom panel we plot the brightness temperature (Chapter 13, by Brosius, summarizes radiative transfer terminology) seen by an observer looking straight down on the dipole. In this panel the solid line represents the  $x$  mode brightness temperature, which the observer will see as one circular polarization (right circular polarization if the spot is of positive magnetic polarity), while the dashed line represents the  $o$  mode (seen by the observer as the opposite circular polarization).

A height of zero in the atmospheric model used for this calculation corresponds to the base of the corona. The density is  $10^{10} \text{ cm}^{-3}$  at the base and decreases exponentially with a scale height of 5000 km. The temperature is 6000 K below the corona and  $1.0 \times 10^6$  K at the base, increasing to  $3.0 \times 10^6$  K at a height of about 15000 km. The morphology of the radio emission can easily be understood by referring to the gyroresonance (GR) layers and the details of the temperature model, and recalling that along any given line of sight we only see down to the highest optically thick layer:

- Neither mode is optically thick in the  $s = 4$  layer, but at the outer edges of this layer there is enough opacity in the  $x$  mode to produce a brightness temperature of order  $10^5$  K, which provides the outer boundary of the radio source.
- On the  $s = 3$  layer, the  $o$  mode is only (marginally) optically thick at the low-lying outer edge of the layer where  $\theta$  is largest, but the temperature is relatively low there because of the low altitude. The  $x$  mode is optically thick in the  $s = 3$  layer to within  $\sim 5000$  km from the center of the umbra, and the peak brightness temperature in the  $x$  mode occurs close to the inner edge of this optically-thick region since the height of the layer, and therefore the temperature, is maximum there.

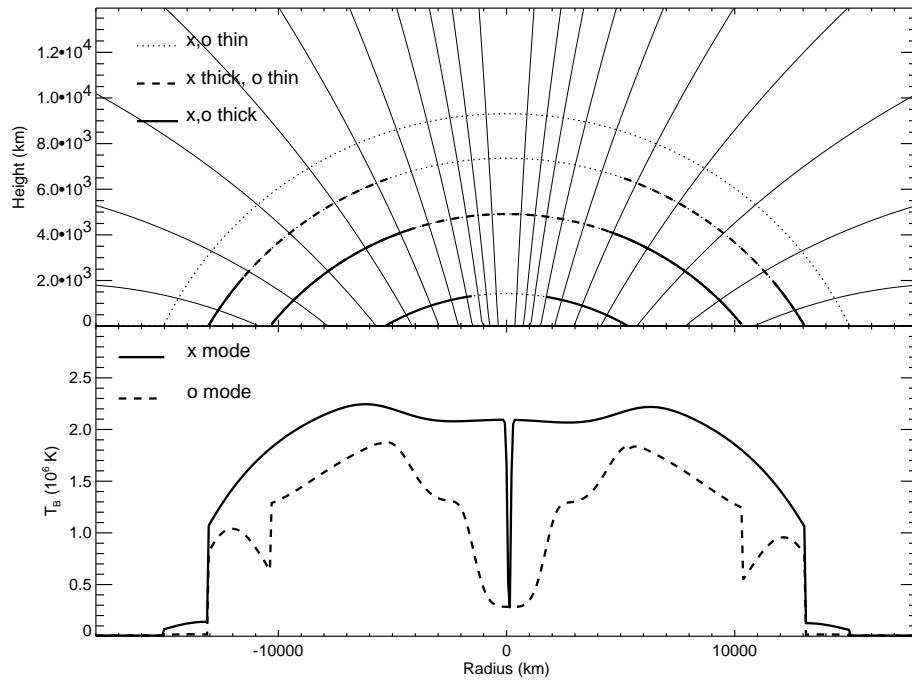


Figure 5.2. Plots of the gyroresonance layers of a dipole sunspot model (upper panel) and the predicted brightness temperatures resulting from an observation of such a spot (lower panel), viewed nearly vertically (actually  $1^\circ$  off vertical). In the upper panel the thin solid lines are magnetic lines of force and the dotted lines are the  $s = 1, 2, 3, 4$  gyroresonance layers, with  $s = 4$  the highest and  $s = 1$  the lowest layer. Where the gyroresonance layers are optically thick (i.e.,  $\tau \geq 1$ ) in the  $o$  mode, they have been overplotted with a thick solid line. Except in the  $s = 1$  layer where the  $x$  mode does not propagate, a layer which is optically-thick in the  $o$  mode is also thick in the  $x$  mode. If a gyroresonance layer is optically thick in the  $x$  mode but not in the  $o$  mode, it is overplotted with a thick dashed line. In the lower panel, the  $x$ -mode brightness temperature is shown by a solid line and the  $o$  mode brightness temperature by a dashed line. The frequency is 5.0 GHz, the dipole is buried at a depth of  $1.2 \times 10^9$  cm, and the maximum field strength at the surface is 2500 G. In the model temperature increases with radial height from  $1.0 \times 10^6$  K at the base of the corona (zero height in this case) to  $3.0 \times 10^6$  K at about 15000 km.

- At smaller radii where the  $s = 3$  layer is optically thin, the main contribution to the  $x$  mode comes from the  $s = 2$  layer which is lower and therefore at a lower temperature: this shows up as a drop in brightness temperature at small radii.
- In the very center of the  $s = 2$  layer where the line-of-sight is along the field line, the  $x$  mode is optically thin and there is a narrow low-

temperature feature. However, it is only a fraction of an arcsecond across and would be difficult to observe.

- In the  $o$  mode the central depression in brightness temperature due to the transparency of the  $s = 2$  layer at small  $\theta$  is much broader, and at the center of the spot even the  $s = 1$  layer is optically thin in the  $o$  mode, but still has sufficient opacity to maintain the brightness temperature at  $3.0 \times 10^5$  K.
- The sharp features in the  $o$  mode profile at radii of order  $10^4$  km are due to the gap between the radius at which the optically thick  $s = 2$  layer drops beneath the corona and the radius at which  $\theta$  increases sufficiently for the  $s = 3$  layer to become (in this case only marginally) optically thick.

## 4.2 The effect of viewing angle

Since the angle  $\theta$  is so important in determining the opacity of a GR layer, changing the viewing angle can have a dramatic effect on the appearance of the radio source and this is shown in Figure 5.3, where we view the same dipolar coronal field at an angle  $20^\circ$  to the vertical. The format of the figure is identical to that of Fig. 5.2 except that the dipole and the surface have been tilted to show them as the observer would see them. On the far side of the spot from the observer (the left side of this figure) the field lines at the outer edge of the GR layers are nearly orthogonal to the line of sight and this leads to a large opacity in both modes in the  $s = 3$  layer there and consequently a relatively small difference in brightness temperature between the two modes. Because the  $s = 3$  layer is optically thick to a greater height on the far side where  $\theta$  is larger, peak brightness temperatures are higher there than on the near side, where the  $o$  mode in particular shows structure due to changes in opacity and differences in temperature between the different layers.

## 4.3 Variation with frequency

The change in appearance of the radio emission as frequency changes may be seen in Figure 5.4, where we plot the radio profiles across the dipolar field viewed from directly above in the  $x$  (upper panel) and  $o$  (lower panel) modes at frequencies from 4 GHz (outermost curve) to 16 GHz (innermost curve) at an interval of 1 GHz. Since higher frequencies correspond to stronger magnetic fields, source size decreases as frequency rises. In the  $o$  mode the sharp edges at the outer boundaries of the  $s = 3$  and  $s = 2$  layers are readily evident, changing in dimension as frequency and correspondingly the appropriate value of magnetic field strength change. In the  $x$  mode the outer edges of the  $s = 3$  and  $s = 4$  layers are evident at lower frequencies, while the outer edge of

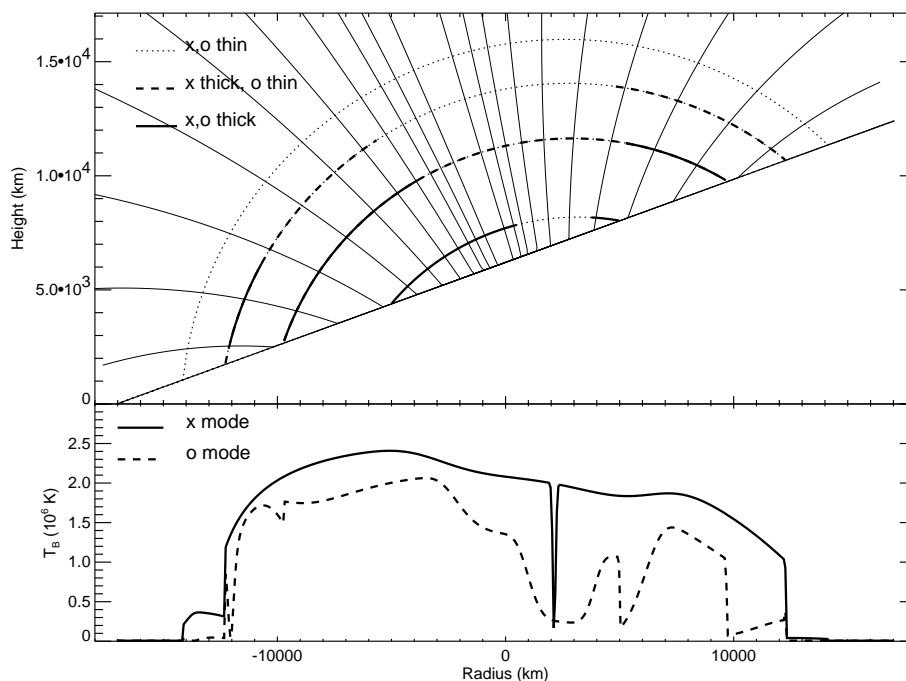


Figure 5.3. A plot in format identical to Figure 5.2, except that now the sunspot is viewed from an angle at  $20^\circ$  to the axis of the dipole (the observer is again at the top of the page). The brightness temperature profiles in the bottom panel are shown as the observer would see them in projection.

the  $s = 2$  layer becomes apparent at higher frequencies. There is a dramatic drop in the peak brightness temperature of the  $x$  mode near the center of the spot when the  $s = 2$  layer drops below the corona, since the  $s = 3$  layer is optically thin at these small viewing angles. The general drop in brightness temperature as frequency rises is due to the fact that at higher frequencies the GR layers are lower in the corona and therefore, in this model, lie in regions of lower temperature.

Spectra at four different radii and the area-weighted spectrum of the whole spot are shown in Figure 5.5. Each individual local  $x$  mode spectrum is fairly smooth at low frequencies where we simply see the third-harmonic GR layer move down the temperature gradient as  $\nu$  and therefore  $B$  increases. The local  $o$  mode spectra show more structure due to the different harmonic resonance layers along each line of sight, while the averaged spectrum shows essentially no structure. In all cases for this model the  $x$  mode is brighter than the  $o$  mode since, on average, the  $x$  mode opacity occurs higher up the temperature gradient. In other models this need not be the case: in situations where the  $x$  mode is

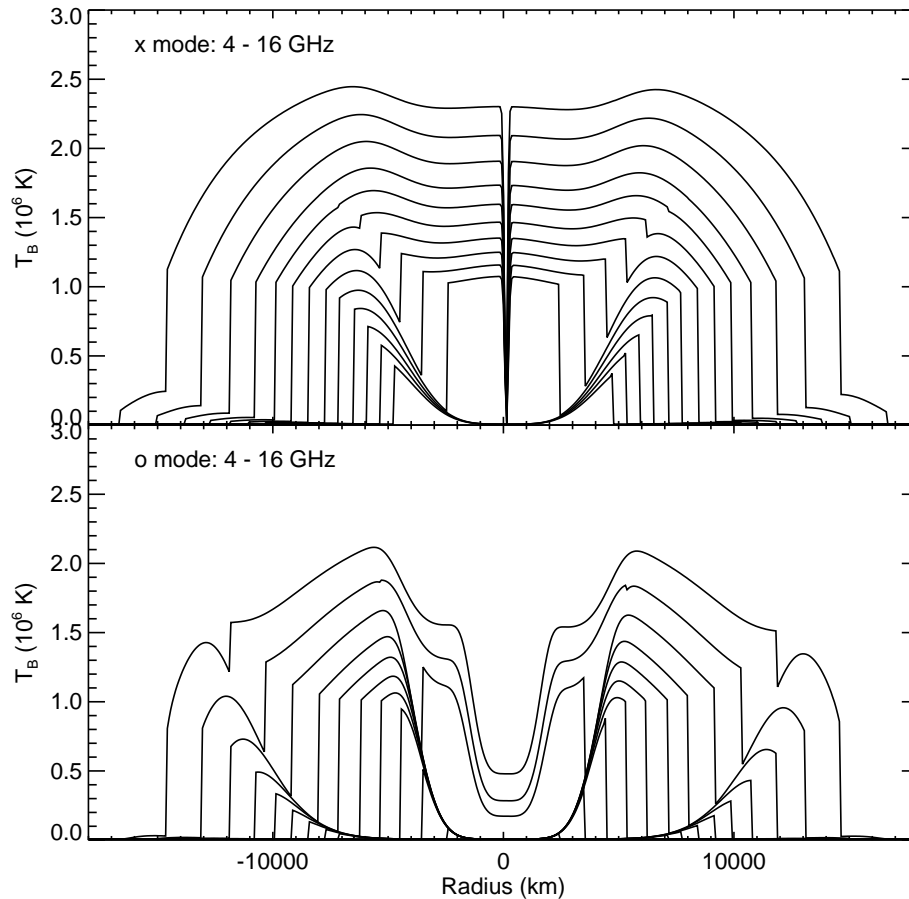


Figure 5.4. Brightness-temperature profiles across the dipole sunspot model of Figure 5.2 at frequencies spaced by 1 GHz from 4 to 16 GHz. The upper panel shows the  $x$  mode profiles and the lower panel the  $o$  mode. In each panel the lowest-frequency profiles are the outside profiles.

optically thick in the  $s = 3$  layer but the highest layer in which the  $o$  mode is optically thick is  $s = 2$ , the overall emission will be polarized in the sense of the  $o$  mode if the temperature structure is such that the deeper  $s = 2$  layer is hotter than the  $s = 3$  layer. Vourlidas (1996) interprets a detection of  $o$  mode polarization from a sunspot in terms of a temperature structure of this type.

The structure revealed at many closely-spaced frequencies in these models shows that appropriate observations contain a great deal of information about both the magnetic field and temperature of the corona. The contrast between the local spectra and the mean spectrum of the spot indicates the value of high spatial resolution in studies of this kind.

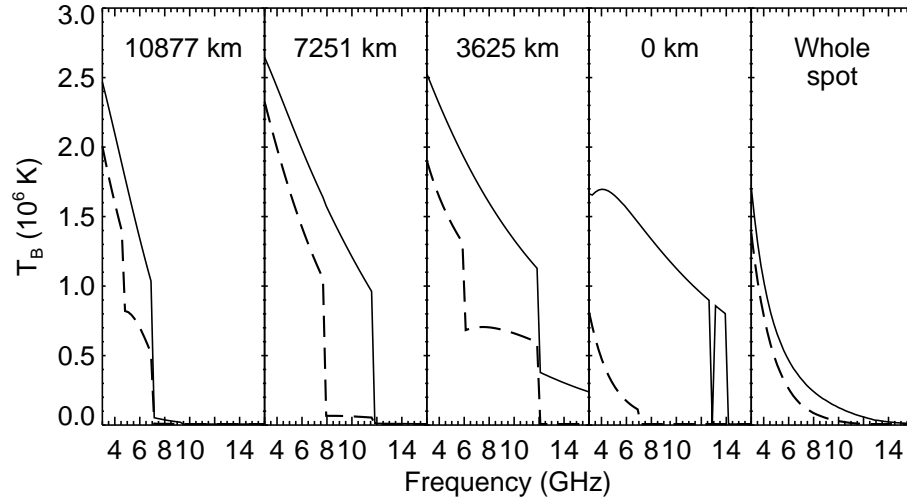


Figure 5.5. Spectra of the brightness temperature at 4 different locations across the spot in Figure 5.4 (first 4 panels) and a spectrum averaged across the whole spot (last panel). The spectra are labelled according to their distance from the center of the spot. The  $x$  mode brightness temperature is plotted with a solid line and the  $o$  mode brightness temperature with a dashed line.

## 5. Observational Examples

We have used a dipolar magnetic field with simple temperature gradients as examples here because they are particularly straightforward to calculate, but the basic principles apply to all gyroresonance emission. Rarely do actual observations show the straightforward structure of our models. Isolated sunspots viewed near the center of the disk can show the basic pattern of a symmetric ring of emission, with low brightness temperatures over the umbra where  $\theta$  is small. An example of profiles from such a sunspot is shown in Figure 5.6, taken from Zlotnik *et al.* (1996).

This is a VLA<sup>1</sup> observation with data at the frequencies 4.5, 5.0, 8.0, 8.4, 14.7 and 15.0 GHz. At the two highest frequencies there are no optically-thick GR layers in the corona and brightness temperatures remain low. In general we see that the brightness temperature decreases steadily as frequency increases, and the  $x$  mode brightness temperature everywhere exceeds the  $o$  mode brightness temperature at the same frequency. As discussed in the previous section, this combination of properties suggests a positive gradient of temperature with height, at least over the range of heights covered by these observations. The

<sup>1</sup>The VLA is a facility of the National Radio Astronomy Observatory, which is operated by Associated Universities, Inc., under cooperative agreement with the National Science Foundation.

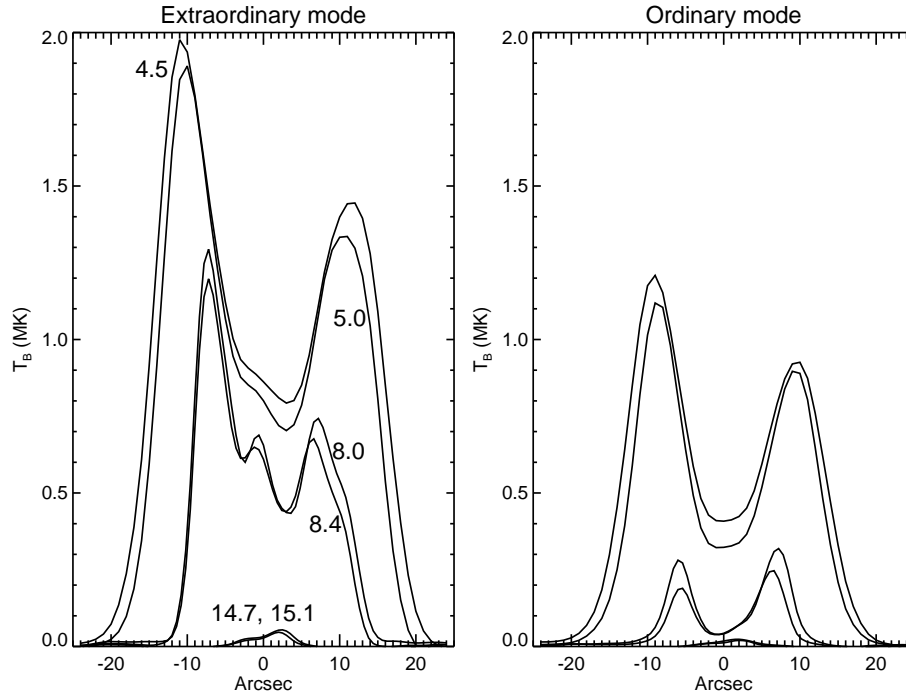


Figure 5.6. Brightness-temperature profiles across an isolated sunspot observed near disk center (actually  $13^\circ$  north-west of disk center) with the VLA by Zlotnik *et al.* (1996). The 6 curves each show the brightness temperature along a cut across the source at a different frequency, starting with 4.5 GHz as the outermost curve, and 14.7 & 15.0 GHz as the two innermost curves. The curves are labelled according to frequency in the left panel which shows the  $x$  mode; the right panel shows the corresponding  $o$  mode profiles, which are present in the same order as in the left panel.

central depression in the  $x$  mode is far broader than the corresponding feature in Fig. 5.4. This can be explained if the temperature has a radial dependence, i.e., the corona over the umbra is cooler than over the penumbra (in Fig. 5.4 the temperature has no radial dependence). Another feature which is not consistent with the simple models is that the radio emission is brighter on the eastern side, closer to disk center, whereas in an atmosphere with a positive temperature gradient viewed at a moderate angle (e.g., Fig. 5.3), we expect the side away from disk center to have brighter radio emission. In these observations, the spatial resolution, although excellent (several arcseconds), is probably inadequate to see the sharp edges at resonance layer jumps seen in Figure 5.4.

Figure 5.7 shows another simple sunspot observed by the VLA at 8.0 GHz, in which a resonance jump may be visible. The sunspot was located  $240''$  west of disk center. The  $x$  mode image is quite round with a relatively flat

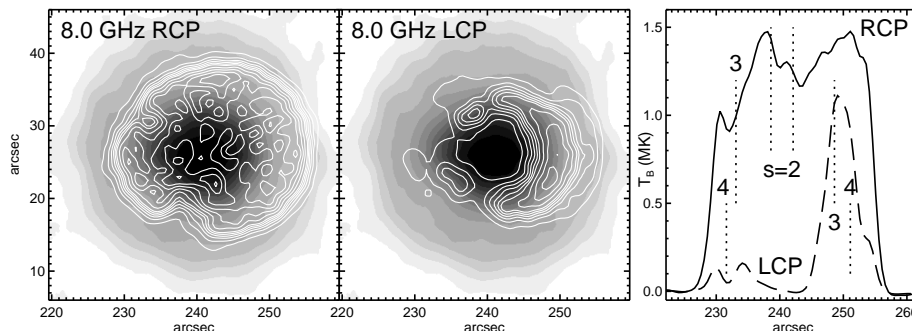


Figure 5.7. VLA observations of a sunspot on 2001 July 17 at 8.0 GHz. The left panel shows contours of right circularly polarized (RCP, the  $x$  mode for this spot) emission superimposed on a white light image, while the middle panel shows contours of left circular polarization (LCP,  $o$  mode) on the white light image. Contours are at brightness temperatures of .05, .15, ..., .55, .75, .95, ...,  $1.75 \times 10^6$  K, and the resolution is  $2''$ . The  $x$  mode is optically thick everywhere, while the  $o$  mode shows the classic ring structure due to the fact that the opacity is low where the line of sight is parallel to the magnetic field direction and increases outwards from that point as the magnetic field lines in the corona fan outwards. The right panel shows horizontal profiles (units of  $10^6$  K) through the radio images at a vertical coordinate of  $25''$  for RCP (solid line) and LCP (dashed line), showing the presence of a number of sharp edges. For comparison, the locations of the  $s = 2, 3$  and  $4$  harmonics along the same path determined from the SOHO/MDI longitudinal magnetogram in the photosphere are marked by vertical dotted lines.

brightness temperature profile across the spot, indicating that it is optically thick everywhere. It shows the typical sharp drop at the outer edges of the source where the gyroresonance layers drop out of the corona. As in Fig. 5.6, the  $x$  mode is everywhere brighter than the  $o$  mode, and the  $x$  mode source is much larger than the  $o$  mode source. The  $o$  mode image shows a nice ring structure that is markedly asymmetric, with the brightest emission on the west side of the spot. This behaviour is in perfect agreement with the earlier models: in the  $o$  mode opacity is lower than in the  $x$  mode, and it is only substantial on the far side of the spot where, by geometry, the angle between  $\mathbf{B}$  and the line of sight is larger because the field lines coming out of the spot fan out as they go upwards. Another interesting feature of the  $o$  mode image is that in addition to the brightest rim of emission to the west of the umbra, there is another fainter rim of emission further west which we can attribute to the next higher harmonic, which is much fainter because it has much less opacity than the lower harmonic.

The examples used here are of simple sunspots since they most closely resemble our model calculation and therefore most straightforwardly illustrate the concepts discussed earlier. Most simple sunspots show considerable structure in the radio emission that does not fit the symmetric patterns of model dipoles, most active regions of interest are far more complicated, and the previous pub-

lished radio images of active regions (too numerous to refer to here: see White *et al.* 1992 for a list of studies published prior to 1992) show the full range of complexity. However, we emphasize that there is no difference in principle between the simple dipole model and a real active region: in the latter, as in the former, it is the interplay between the the structure of the GR layers (particularly the variation of  $\theta$  over the layers) and the temperature and density structure of the corona that determines the appearance of an active region at microwave frequencies. Much of the diagnostic potential of gyroresonance emission lies in the fact that at a given frequency it reveals specific well-defined layers, and this is equally true of simple dipolar sunspots and real active regions with more convoluted GR layers.

## 6. Applications of Gyroresonance Emission

### 6.1 Coronal magnetic field measurement

One of the simplest uses of radio observations is the determination of magnetic field strengths at the base of the corona (e.g., Hurford 1986). The absolute value of the coronal magnetic field strength is important for understanding the energetics of the corona, and the availability of free energy stored in coronal magnetic fields which may be used in flares and coronal heating. Figs. 5.2–5.5 demonstrate that where the optically-thick GR layer corresponding to a given frequency and mode drops below the corona, the radio brightness temperature at that frequency and corresponding polarization shows a sharp drop from coronal to approximately chromospheric values. (Note that the transition region is not expected to be detected via gyroresonance emission if its thickness is less than  $1''$  as energy balance models predict, because its signature would be confined to the line at the intersection of the  $< 1''$ -thick surface of the transition region with the typically  $< 0''.2$ -thick GR surface, and the thickness of this line is likely to be so narrow as to be undetectable.) Observationally it is a simple matter to detect such a signature. Thus the locations of the outer edges of the radio sources at differing frequencies contain information on the magnetic field strength at the base of the corona. With data such as those shown in Figs. 5.4–5.5, several harmonics can be identified unambiguously in each mode and therefore the appropriate values of  $s$  can be identified, which is essential to determine absolute values of  $B$ . In this way, it is straightforward to map the distribution of  $B$  over the base of the corona wherever the radio emission is dominated by bright gyroresonance emission. This technique has been convincingly demonstrated with the Owens Valley Solar Array (Gary & Hurford 1994).

When only a few frequencies are available, as in VLA observations such as Figure 5.8, it is possible to map the extent of the region in the corona in which the magnetic field exceeds the values which correspond to the frequencies observed. High-frequency observations allow us to estimate the maximum

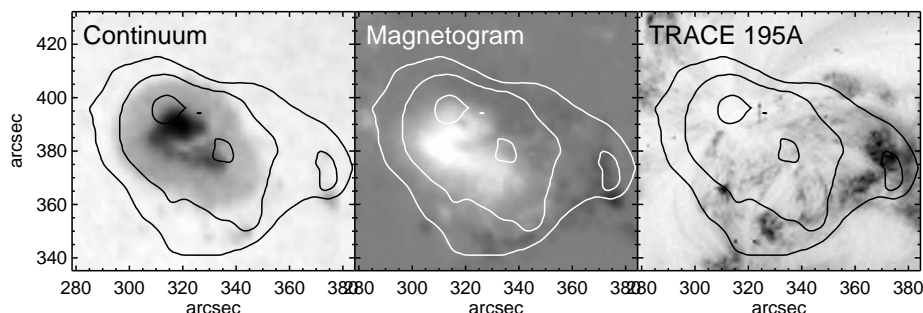


Figure 5.8. Contours of magnetic field strength at the base of the corona plotted on white light (left), magnetogram (middle) and TRACE 195 Å Fe XII (right) images of a sunspot observed on 1999 May 13. The coronal contours are plotted at 500, 900 and 1700 G, corresponding to the radio images at 4.5, 8.0 and 15.0 GHz used to construct the coronal magnetogram. Note the displacement of the 1700 G coronal magnetic field strength from the strongest photospheric fields, due in part to projection effects resulting from the height of the radio-emitting layer. Axes are labelled in arcseconds from apparent disk center.

magnetic field strength in the corona. This can be obtained from the maximum frequency  $\nu_m$  GHz at which coronal brightness temperatures are observed, using the assumption that this will take place in the  $x$  mode in the  $s = 3$  layer at the base of the corona where the field strength is maximum. (One feature illustrated by Figure 5.1 is that only in extreme conditions is the  $s = 4$  layer optically thick, and therefore  $s = 3$  is generally appropriate for this purpose.) On this assumption, the maximum field strength is  $120 \nu_m$  G. For example, if as in White *et al.* (1991) there are coronal brightness temperatures at 15 GHz, the coronal magnetic field must reach at least 1800 G. When the 17 GHz Nobeyama radioheliograph measures coronal brightness temperatures from an active region, the coronal magnetic field must exceed 2000 G (Shibasaki *et al.* 1994). When many closely-spaced frequencies have been observed, as is possible with the Owens Valley Solar Array and RATAN-600, fairly tight limits can be placed on the maximum magnetic field strength (Akhmedov *et al.* 1982; Lee *et al.* 1993; Gary & Hurford 1994).

A common argument applied to coronal magnetic field strengths is as follows: magnetic flux in the (high- $\beta$ ) solar photosphere tends to be concentrated in small regions of intense (kG) field strength. As this flux rises into the low- $\beta$  solar corona it will expand laterally, thus diminishing the strength of the field. This argument is the basis for the wide-spread belief that coronal magnetic fields are much weaker than the fields measured in the photosphere. The argument appears to be valid for the quiet-Sun fields concentrated in small flux tubes in the cell network: if these fields reached the solar corona with strengths of order of hundreds of G or more, we would see clear signatures in radio images

of the Sun in the form of features over the network at coronal temperatures. Such signatures are not seen (e.g., Gary *et al.* 1990). However, present upper limits for magnetic field strengths in the corona above quiet-Sun regions are well above the field strengths expected from the flux expansion argument.

On the other hand, the argument does not apply to active regions fields. Field strengths of 2000 G or more can be found in the corona, particularly over large sunspots (Shibasaki *et al.* 1994): in active regions there is so much flux that there is little field-free volume to expand into, and so field strength declines much less rapidly with height than simple models tend to predict (Akhmedov *et al.* 1982). The example in Fig. 5.8 shows a coronal magnetogram deduced from VLA data and therefore suffering from poor resolution in  $B$ . In this particular sunspot the maximum line-of-sight field in the photosphere is not much more than 2000 G, yet coronal fields of 1800 G are found to be present in the VLA observations. The recent coronal line measurements above active regions at the limb agree with this conclusion (Lin *et al.* 2000), as does the fact that loop width measurements find that coronal loops tend to have constant widths, rather than showing expansion at greater heights (McClymont & Mikić 1994, Klimchuk 2000).

## 6.2 Simulations of FASR magnetic field measurements

The crude coronal magnetogram shown in Figure 5.8, with just 3 contours from 600 to 1800 G, is the best we can do with VLA data due to the limited number of discrete frequencies available for observations. The Frequency Agile Solar Radiotelescope (FASR) will make images of solar active regions at high spatial resolution at many different frequencies simultaneously, in order to be able to measure coronal magnetic fields continuously over a broad range of field strengths. Gary, Lee, Giordano & Mok (2004, in preparation) have demonstrated how to convert such observations into measurements of the coronal field strength at the base of the corona by resolving the ambiguities of harmonic number. As described above, sharp jumps in the brightness temperature along a given line of sight are expected if where a harmonic layer drops out of the corona. Thus sharp drops in the brightness temperature spectra indicate harmonic numbers. If two such sharp edges are present along a given line of sight then the ratio of the frequencies of the two edges provides a unique identification of the harmonics corresponding to both edges, because we can safely assume that they are adjacent harmonics in the ratio of 2:1, 3:2 or 4:3. It is a great advantage that we can measure spectra in both the  $x$  and the  $o$  modes as opposite circular polarizations, because different edges may appear in either polarization.

This approach has been tested using a physical model of an active region. The model is a potential field model extrapolated from an actual vector magne-

togram. The thermal structure (density and temperature as a function of position throughout the volume) was computed self-consistently assuming a plasma heating model in which the volumetric heating rate is directly proportional to the local magnetic field strength (Mok *et al.* 2004). Given a three-dimensional model, we can simply predict the radio emission that would be observed. The radio images are folded through the FASR instrument response function, adding a realistic noise level. Maps at 100 frequencies are produced and the spectra analyzed on a point by point basis.

Examples of the resulting spectra are shown in Figure 5.9. In both these cases, one sharp edge is detected in each polarization and the two edges have a frequency ratio of 2:1, implying that they are the first and second harmonics. Once the harmonic number and the frequency of the edge are known, the magnetic field at the base of the corona is uniquely determined. It is straightforward to apply this method to two-dimensional data, as shown in Figure 5.10. The agreement between the input model fields and the values derived from realistic radio data is excellent.

### 6.3 Coronal currents

An extension of this simple measurement is the identification of coronal currents. Coronal currents occur in regions of highly sheared magnetic fields and therefore elevate coronal field strengths above the values expected from simple potential-field (i.e., current-free) extrapolations of surface measurements. They will also produce a characteristic reversal of field direction with position as one moves across the current layer. Both these features are in principle observable in radio images. Relatively little has been done in this area due to the difficulties of obtaining well-calibrated, unsaturated photospheric magnetogram data simultaneous with suitable radio data (i.e., at high spatial resolution and covering the appropriate frequency range), and the problem of identifying the height of the radio source (Alissandrakis *et al.* 1980; Schmahl *et al.* 1982; Alissandrakis & Kundu 1984; Chiuderi Drago *et al.* 1987; Schmelz *et al.* 1994). Figure 5.11 shows an example of the radio emission from a complex of sunspots at three different frequencies. The three frequencies correspond to three different magnetic field strengths: these are  $x$  mode images corresponding to the 450 G surface at 5 GHz, 750 G at 8.4 GHz and 1350 G at 15 GHz (these correspond to the fourth harmonic surface being optically thick since the temperature in the corona was very high for this active region). Note that, as should be the case, the optically thick region becomes smaller at higher frequencies corresponding to larger magnetic field strengths. At the lower frequencies the optically thick surface covers the whole active region; at the highest frequency several discrete sources are found. One of them (the bright source in the center of panel *d*, over the neutral line) has been shown to be the result of highly non-potential

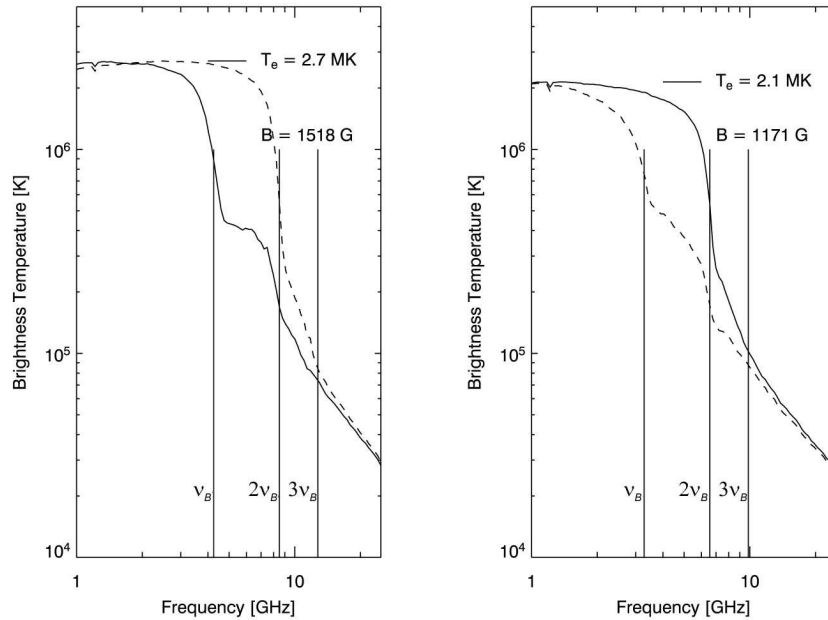
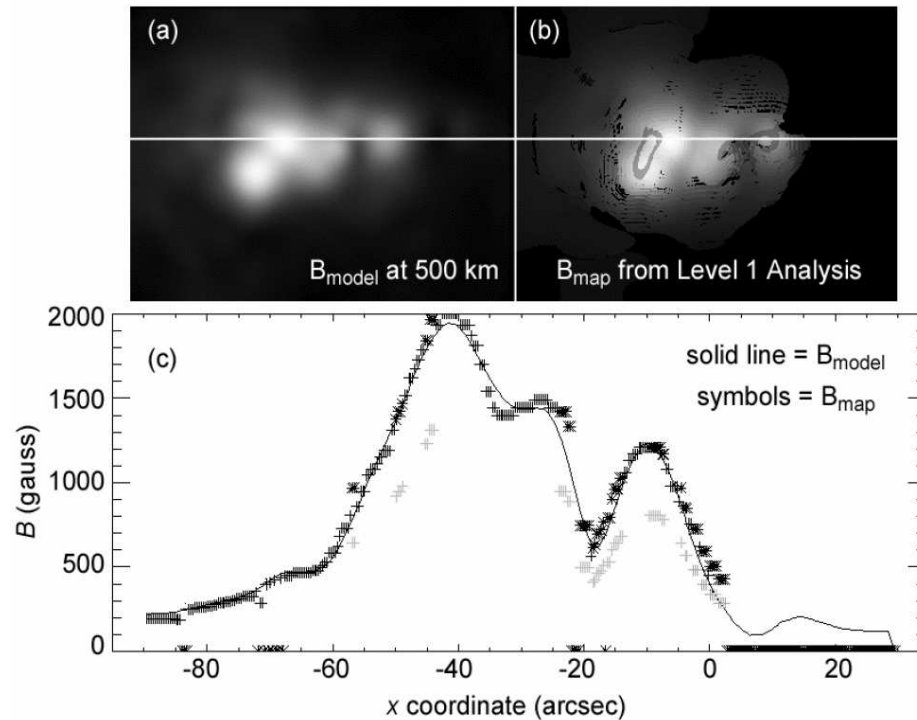


Figure 5.9. Two examples of radio spectra arising from the thermal active region model of Mok *et al.* (2004). The solid line is for one sense of circular polarization and the dashed line is for the opposite polarization: in the left panel the dashed line is the  $x$  mode, while in the right panel it is the  $o$  mode. In both cases the harmonic ratio is 2:1, allowing identification of the magnetic field in each case as labelled; fiducial vertical lines indicating the locations of the harmonics are shown on each panel.

fields at this location (Lee *et al.* 1997). Potential extrapolations of photospheric magnetic fields were unable to explain the presence of a 15 GHz radio source at this location above a neutral line even with the conservative assumption that the 4th harmonic layer could have sufficient opacity to be optically thick (requiring 1330 G fields). In this case a photospheric vector magnetogram also indicates the presence of a strong current with footpoints in the photosphere on either side of the neutral line and consistent with a coronal current crossing the neutral line in the corona at the location inferred from the radio data.

#### 6.4 Tests of magnetic extrapolations

Extrapolations of magnetic field measurements from the lower atmosphere into the corona are likely to become an increasingly important tool in the near future, and in conjunction with the radio measurements are expected to provide a powerful means for studying coronal fields. One important area where the techniques interact is in testing extrapolation algorithms: as described earlier,



*Figure 5.10.* The results of applying the gyroresonance technique to model data. The top left panel shows the magnetic field in the input model at a height of 500 km, representative of the base of the corona (in the thermal model the actual height of the base of the corona varies). The top right panel shows the values derived from the radio technique of identifying harmonics from spectra in each pixel and using the frequency ratio to determine the harmonic numbers. The lower panel shows a more detailed comparison of the model (line) and radio-derived (symbols) fields along the horizontal line in the upper panels. The technique occasionally fails when edges are not sufficiently sharp and a 3:2 ratio can be mistaken for a 2:1 ratio (grey symbols). From Gary, Lee, Giordano & Mok (2004, in preparation).

extrapolation is a very difficult procedure and many different approaches have been tried. It is clearly valuable to be able to test the success of a given extrapolation technique, and radio data provide one way of doing so. The preceding subsection described such tests involving magnetic field strengths. Another important test involves the topology of magnetic field lines derived from the extrapolations. For the same region described above, Lee *et al.* (1999) compared the temperatures measured on the same field lines at two different frequencies, corresponding to two different locations (field strengths) on the same field lines. Since heat transport parallel to the magnetic field is so much faster than it is across magnetic field lines, one expects that temperatures measured at two different locations on a field line should be very well correlated. Lee *et al.* (1999)

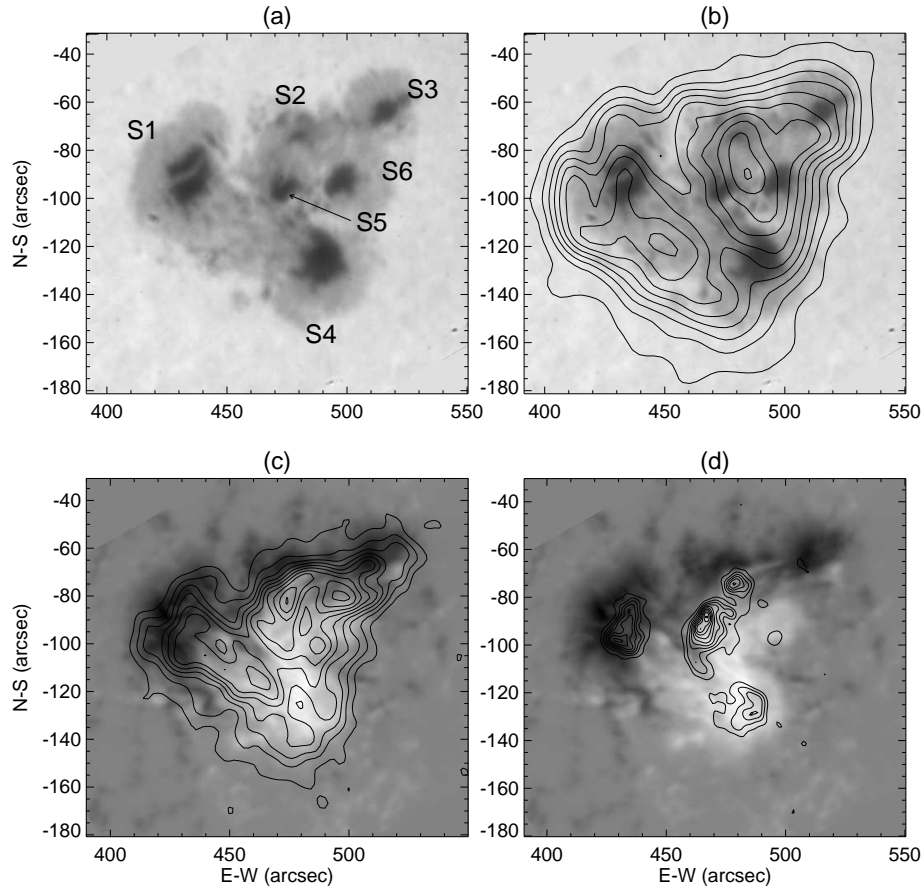


*Figure 5.11.* VLA observations of a complex solar active region reflecting the magnetic field and temperature distribution in the corona over the active region. The white-light image (a) shows a number of spots within the same penumbra. In panel (b) contours of the VLA 5 GHz emission are overlaid on the white-light image: since the radio emission is due to the gyroresonance process, the radio image corresponds to the electron temperature distribution on the surface in the corona where the magnetic field  $B$  equals 450 G. Panels (c) and (d) show contours of the 8.4 GHz ( $B = 750$  G) and 15 GHz emission ( $B = 1350$  G), respectively, overlaid on a longitudinal photospheric magnetogram which indicates the direction of the magnetic field at the surface (white = upgoing, black = downgoing field). The maximum brightness temperatures in the radio images are  $4.4 \times 10^6$  K at 4.9 GHz,  $4.6 \times 10^6$  K at 8.4 GHz, and  $1.8 \times 10^6$  at 15 GHz, respectively. Contours begin at 10% of the maximum brightness temperature and then are 10% apart. From Lee *et al.* (1997).

compared this correlation for the field lines from potential, linear force-free and nonlinear force-free extrapolations using brightness temperatures measured at 5 and 8 GHz and showed that indeed the correlation was extremely good for the nonlinear force-free extrapolation and much poorer for the other extrapo-

lations. The radio data were also useful for resolving the well-known problem of the  $180^\circ$  ambiguity in the vector magnetogram measurements. The techniques of radio measurements and surface extrapolations, particularly when better chromospheric magnetograms become available, are expected to provide complementary information necessary to study coronal magnetic fields.

## 6.5 Heights of radio sources

Perhaps the major shortcoming of gyroresonance emission as a diagnostic is the fact that it does not yield height information directly. (Other coronal diagnostics such as X-ray imaging share this shortcoming.) A single radio observation at multiple frequencies is sensitive to emission from many different GR layers in the corona, but is largely insensitive to the distance between the layers, and for this reason does not easily lend itself to height determination. When two observations at different times are combined, the change in perspective produced by solar rotation permits stereoscopy to be used to estimate source heights (Aschwanden & Bastian 1994). However, to carry this out correctly for gyroresonance emission requires both that the physical properties of the corona not change between the observations and that the changes in appearance expected from the dependence on  $\theta$  be taken into account carefully, which is far from trivial.

In principle there is information present on the heights of the GR layers due to the dependence of the optical depth (5.1) on  $L_B$ , and the fact that we know the magnetic field strength in each layer.  $L_B$  must be consistent with the height separation of isogauss layers of different field strengths. If  $L_B$  could be determined from the data, it may be possible to use the combination of  $L_B$ , the fundamental law  $\nabla \cdot \mathbf{B} = 0$  and the fact that  $B$  is constant within a layer to reconstruct the heights of the GR layers, at least approximately. However, in (5.1),  $L_B$  is coupled with the electron density, and it may be difficult to separate these two parameters from radio data alone: EUV observations which provide independent information on  $n_e$ , and improved extrapolations of surface fields which provide an estimate of  $L_B$ , may help with this separation.

## 7. Summary

This chapter has reviewed the radio technique of using gyroresonance emission to measure magnetic field strengths in the solar corona. These measurements have the potential to determine fields in solar active regions above field strengths of order 200 G, and thus provide important information for studying changes in coronal magnetic fields and their role in flares, eruptions and coronal heating. A major advance in the application of this technique will be provided by the construction of the Frequency Agile Solar Radiotelescope, which is being designed to make routine high-resolution coronal magnetic field measurements

as one of its primary science goals. In addition, the data acquired by FASR will be ideal for going beyond the techniques described here and starting to exploit the full extent of the three-dimensional information present in the radio data.

### Acknowledgments

Solar research at the University of Maryland is supported by NSF grants ATM 99-90809 and ATM 02-33907 and NASA grants NAG 5-11872, NAG 5-12860 and NAG 5-10175.

### References

- Akhmedov, Sh. B., Gelfreikh, G. B., Bogod, V. M., & Korzhavin, A. N. 1982, *Solar Phys*, 79
- Alissandrakis, C. E. & Kundu, M. R. 1984, *A&A*, 139, 271
- Alissandrakis, C. E., Kundu, M. R., & Lantos, P. 1980, *A&A*, 82, 30
- Amari, T., Boulmezaoud, T. Z., & Mikic, Z. 1999, *A&A*, 350, 1051
- Aschwanden, M. J. & Bastian, T. S. 1994, *ApJ*, 426, 425
- Bornatici, M., Cano, R., de Barbieri, O., & Engelmann, F. 1983, *Nucl. Fusion*, 23, 1153
- Bray, R. J. & Loughhead, R. E. 1964, *Sunspots*, Chapman & Hall, London
- Brosius, J. W. & Holman, G. D. 1989, *ApJ*, 342, 1172
- Chiuderi Drago, F., Alissandrakis, C. E., & Hagyard, M. 1987, *Solar Phys*, 112, 89
- Gary, D. E. & Hurford, G. J. 1994, *ApJ*, 420, 903
- Gary, D. E., Zirin, H., & Wang, H. 1990, *ApJ*, 355, 321
- Gary, G. A. 1989, *ApJ Supp.*, 69, 323.
- Gelfreikh, G. B. & Lubyshev, B. I. 1979, *Sov. Astron.*, 23, 316
- Ginzburg, V. L. & Zheleznyakov, V. V. 1961, *Sov. Astron.*, 5, 1
- Hurford, G. J. 1986, in *Solar Flares and Coronal Physics Using P/OF as a Research Tool*, (Tandberg-Hanssen, E., Wilson, R. M., and Hudson, H. S., eds.), NASA Conf. Pub. 2421, 191
- Jiao, L., McClymont, A. N., & Mikić, Z. 1997, *Solar Phys*, 174, 311
- Kakinuma, T. & Swarup, G. 1962, *ApJ*, 136, 975
- Klimchuk, J. A. 2000, *Solar Phys*, 193, 53
- Klimchuk, J. A. & Canfield, R. C. 1994, in *Solar Active Region Evolution: Comparing Models with Observations*, (Balasubramanian, K. S. & Simon, G. W., eds.), PASP Conf. Ser. 68, 233
- Krüger, A., Hildebrandt, J., & Fürstenberg, F. 1985, *A&A*, 143, 72
- Lantos, P. 1972, *Solar Phys*, 22, 387
- Lee, J., McClymont, A. N., Mikić, Z., White, S. M., & Kundu, M. R. 1998, *ApJ*, 501, 853

- Lee, J., White, S. M., Gopalswamy, N., & Kundu, M. R. 1997, *Solar Phys*, 174, 175
- Lee, J., White, S. M., Kundu, M. R., Mikić, Z., & McClymont, A. N. 1999, *ApJ*, 510, 413
- Lee, J. W., Hurford, G. J., & Gary, D. E. 1993, *Solar Phys*, 144, 45
- Lin, H., Penn, M. J., & Tomczyk, S. 2000, *ApJ*, 541, L83
- McClymont, A. N. & Mikić, Z. 1994, *ApJ*, 422, 899
- Melrose, D. B. 1980, *Plasma Astrophysics*, Gordon and Breach, New York
- Metcalf, T. R., Jiao, L., McClymont, A. N., Canfield, R. C., & Uitenbroek, H. 1995, *ApJ*, 439, 474
- Mok, Y., Lionello, R., Mikić, Z., & Linker, J. A. 2004, *ApJ*, submitted.
- Robinson, P. A. 1991, *Solar Phys*, 136, 343
- Robinson, P. A. & Melrose, D. B. 1984, *Aust. J. Phys.*, 37, 675
- Schmahl, E. J., Kundu, M. R., Strong, K. T., Bentley, R. D., Smith, J. B., & Krall, K. R. 1982, *Solar Phys*, 80, 233
- Schmelz, J. T., Holman, G. D., Brosius, J. W., & Willson, R. F. 1994, *ApJ*, 434, 786
- Semel, M. & Skumanich, A. 1998, *A&A*, 331, 383
- Shibasaki, K., Enome, S., Nakajima, H., Nishio, M., Takano, T., Hanaoka, Y., Torii, C., Sekiguchi, H., Kawashima, S., Bushimata, T., Shinohara, N., Koshiishi, H., Shiomi, Y., Irimajiri, Y., Leka, K. D., & Canfield, R. C. 1994, *Publ. Astron. Soc. Japan*, 46, L17
- Vourlidas, A. 1996, Ph. D. thesis, New Mexico Inst. of Mining and Technology, unpublished.
- White, S. M. & Kundu, M. R. 1997, *Solar Phys*, 174, 31
- White, S. M., Kundu, M. R., & Gopalswamy, N. 1991, *ApJ*, 366, L43
- White, S. M., Kundu, M. R., & Gopalswamy, N. 1992, *ApJ Supp.*, 78, 599
- Zheleznyakov, V. V. 1962, *Sov. Astron. J.*, 6, 3
- Zheleznyakov, V. V. 1970, *Radio Emission of the Sun and the Planets*, Pergamon Press Ltd., Oxford
- Zlotnik, E. Ya. 1968*a*, *Sov. Astron.*, 12, 245
- Zlotnik, E. Ya. 1968*b*, *Sov. Astron.*, 12, 464
- Zlotnik, E. Ya., Kundu, M. R., & White, S. M. 1996, *Radiophysics and Quantum Electronics*, 39, 255